Article

Not peer-reviewed version

Derivation and Experimental Validation of a Parameterized Nonlinear Froude-Krylov Force Model for Heaving Point Absorber Wave Energy Converters

Houssein Yassin *, Tania Demonte Gonzalez, Gordon Parker *, Giorgio Bacelli, Carlos Michelen

Posted Date: 11 April 2025

doi: 10.20944/preprints202504.0893.v1

Keywords: wave energy converter; hydrodynamic modeling; nonlinear hydrodynamics; excitation force; froude-krylov force; point absorber

 doi:10.20944/preprints202504.0893.v1

Article

Derivation and Experimental Validation of a Parameterized Nonlinear Froude-Krylov Force Model for Heaving Point Absorber Wave Energy Converters

Houssein Yassin [1,*,†,‡], Tania Demonte Gonzalez [1,‡], Gordon Parker [1,‡], Giorgio Bacelli [2] and Carlos Michelen [2]

[1] Michigan Technological University
[2] Sandia National Laboratories
* Correspondence: hyassin@mtu.edu
† Current address: Michigan Technological University, Houghton, MI 49931.
‡ These authors contributed equally to this work.

Abstract: Wave energy converters (WECs) have gained significant attention as a promising renewable energy source. Optimal control strategies, crucial for maximizing energy extraction, have traditionally relied on linear models based on small motion assumptions. However, recent studies indicate that these models do not adequately capture the complex dynamics of WECs, especially when large motions are introduced to enhance power absorption. The nonlinear Froude-Krylov (FK) forces, particularly in heaving point absorbers with varying cross-sectional areas, are acknowledged as key contributors to this discrepancy. While high-fidelity computational models are accurate, they are impractical for real-time control applications due to their complexity. This paper presents a parameterized approach for expressing nonlinear FK forces across a wide range of point absorber buoy shapes inspired by implementing real-time, model-based control laws. The model was validated using measured force data for a stationary spherical buoy subjected to regular waves. The FK model was also compared to a closed-form buoyancy model, demonstrating a significant improvement, particularly with high-frequency waves. Incorporating a scattering model further enhanced force prediction, reducing error across the tested conditions. The outcomes of this work contribute to a more comprehensive understanding of FK forces across a broader range of buoy configurations, simplifying the calculation of the excitation force by adopting a parameterized algebraic model and extending this model to accommodate irregular wave conditions.

Keywords: wave energy converter; hydrodynamic modeling; nonlinear hydrodynamics; excitation force; froude-krylov force; point absorber

1. Introduction

The escalating global demand for clean and sustainable energy sources has fueled extensive research to harness the vast potential of ocean waves. With its consistent availability, wave energy is an attractive renewable resource. Site evaluations have confirmed the potential for ocean wave energy resources [1]. Among the various technologies developed, point absorber wave energy converters (PAWEC) have emerged as promising devices capable of efficiently capturing and converting wave energy into electrical power [2]. PAWECs, characterized by buoyant structures tethered to the seabed, offer adaptability to varying wave conditions. The wave-induced vertical motion of its buoyant platform is translated into useful work through a power take-off that can act as either a generator or actuator.

The successful implementation of PAWECs depends on carefully considering design aspects, including buoy size, shape, and mass distribution. Material selection must account for the harsh marine environment, and placement is critical, influenced by factors such as water depth and distance

 doi:10.20944/preprints202504.0893.v1

from the shore. Advancements in control systems enable adaptive strategies that maximize energy extraction under varying wave conditions. Improving PAWEC control mechanisms stands out as a crucial avenue with immense potential to improve the feasibility of wave energy utilization [3]. Recent advances highlight the importance of refined control methods, which demonstrate their ability to increase power absorption by up to 20% while simultaneously reducing structural loads [1].

Extensive research on energy-optimal control, particularly for buoy geometries, has been explored. Topics include: establishing upper bounds for energy extraction [4–6], impedance matching control [6–10], and exploring both closed-form [11,12] and numerical optimal control solutions [13] such as Model Predictive Control (MPC) [14–17]. A common theme is the importance of using accurate WEC math models for analysis and control design. Initially, research focused on buoy response regimes that could be approximated using linear differential equations, valid under the assumption of small motion amplitudes. However, a recent shift toward addressing the nonlinear response of buoys [18–20] is underway to improve energy extraction, particularly when the objective is to increase power production.

Computational fluid dynamics (CFD) models can accurately capture these nonlinearities, but their application in model-based real-time control laws is impractical [21]. A previous investigation [22] comparing various modeling approaches showed that an important nonlinearity comes from the Froude-Krylov (FK) force, particularly for axisymmetric buoys with varying cross-sectional areas. This insight underscores the importance of understanding and incorporating the nonlinear effects of FK forces in the modeling process to develop effective control strategies.

The FK forces arise from the pressure field around a submerged or partially submerged body as it moves through waves. Specifically, they are associated with the nonlinear effects induced by the varying shape and submersion of the structure. Together with the scattering forces, they constitute the entire non-viscous force exerted on a floating body subjected to regular waves [23]. Developing closed-form, computationally efficient FK force expressions is advantageous for implementing real-time, model-based control strategies. This is especially true for buoys whose shapes result in nonlinear FK forces.

Closed-form nonlinear FK force models have been derived in previous studies [24–26], aimed explicitly at using buoy shape effects in model-based control laws for large-motion, nonlinear operating regimes. Giorgi et al. [24] developed a method for generating closed-form FK force expressions using Airy's wave theory to approximate the pressure on a buoy in regular waves. It has recently been used for model-based control solutions, including sliding model control [27], feedback linearization [28], and latching control [21,29,30].

These studies have taken advantage of various buoy shapes, ranging from conventional spheres and cylinders to more unconventional geometries such as the double cone-shaped buoy [18,28]. The FK force approach by Giorgi et al. has been extended in this paper [24] in several ways, including considering flat bottomed buoys, irregular waves, and a parametrization of a large class of buoy shapes using three parameters. Parameterization allows for rapid evaluation of different geometries, making shape optimization efficient. By generalizing the FK force form, this work provides a powerful tool for improving the design and control of wave energy converters. Furthermore, this paper compares the nonlinear FK model with the buoyancy force approach often used in model-based control [18]. Experiments are used to assess model performance using a spherical buoy subjected to regular waves at several frequencies and amplitudes.

The paper is organized as follows. The model form is introduced in Section 2, including the distinction between the buoyancy and Froude-Krylov terms that are derived in Sections 3 and 4. Examples of these terms are compared in Section 5, followed by the experimental validation study in Section 6. Some concluding remarks are provided in Section 7.

 doi:10.20944/preprints202504.0893.v1

2. System Description

Consider the axisymmetric buoy constrained to heave attached by a PTO to the sea floor in Figure 1. In the configuration shown, the buoy has a positive displacement $\zeta(t)$ of its draft line relative to the still-water line. The wave elevation, $\eta(t)$, is also positive in the figure and is assumed to have the general form of Eq. 1 that allows analysis of both regular and irregular waves.

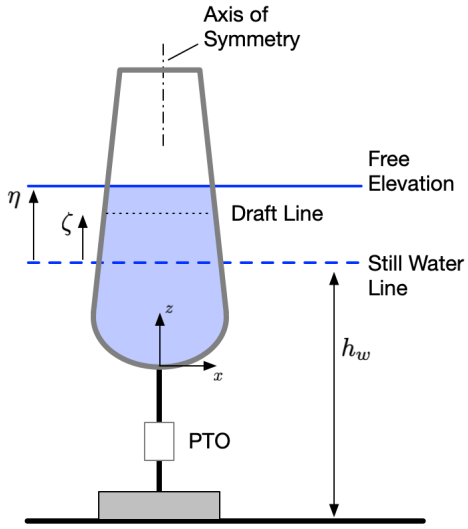

Figure 1. Illustration of an axisymmetric buoy and the notation used for its model.

$$\eta(x,t) = \sum_{i=1}^{n} A_i \sin(\phi_i + \chi_i x - \omega_i t) = \sum_{i=1}^{n} \eta_i \tag{1}$$

where η's ith component has an amplitude, wave number, angular frequency, and phase shift denoted A_i, χ_i, ω_i, and ϕ_i. The wavelengths, $\lambda_i = 2\pi/\chi_i$, are assumed to be large compared to the maximum buoy radius, and therefore the free elevation is considered to be locally horizontal, as shown in Figure 1. A body-fixed coordinate system (x, y, z) is referenced at the bottom of the buoy. The constant water depth, h_w, is the distance from the sea floor to the still water line and is assumed to be large, though it is shown as small in the figure.

Two model variants will be compared, both having the general form of Eq. 2

$$M\ddot{\zeta} = F_P + F_g + F_S + F_R + F_{PTO} \tag{2}$$

where M is the buoy's mass. Assuming that the buoy does not affect the wave field, the pressure exerted on the buoy by the water is denoted F_p, and the buoy weight is F_g. The scattering force, F_S, when combined with the Froude-Krylov force, is called the diffraction force, F_D, [31] and captures the effect of wave distortion around a fixed buoy [6]. The radiation force, F_R, is due to the energy transfer between the buoy and the water as the buoy moves. Finally, F_{PTO} is the power take-off force that adds or removes buoy energy.

The two model variants shown in Eq. 3 are distinguished by how the $F_p + F_g$ term of Eq. 2 is treated. In one case, they are replaced by the Froude-Krylov force $F_{fk} = F_P + F_g$, and in the other by the buoyancy force $F_b = F_P + F_g$.

$$M\ddot{\zeta} = F_{fk} + F_S + F_R + F_{PTO} \tag{3a}$$

$$M\ddot{\zeta} = F_b + F_S + F_R + F_{PTO} \tag{3b}$$

In both cases, the $F_P + F_g$ term will be expressed in a parametric form where a wide range of buoy shapes can be represented using only three independent quantities. In addition, the advantages and disadvantages of the F_{fk} and F_b approaches are discussed. The most significant distinction between

 doi:10.20944/preprints202504.0893.v1

them is the assumed motion of the buoy. The F_{fk} derivation assumes small motions, while the F_b approach does not.

3. Derivation of F_{fk}

The derivation of F_{fk} begins by developing the pressure field for irregular waves. The parameterization of the buoy shape is considered next, followed by a representation of F_{fk} in compact form.

3.1. Pressure

The FK term of Eq. 3a, is the integration of the water pressure field, $\vec{P}(x,z,t)$, over the instantaneous wetted surface of the buoy, S, illustrated by the blue shaded region of Figure 2

$$F_{fk} = F_g - \int\int \vec{P}(x,z,t) \cdot \hat{n}\, dS \tag{4}$$

where $\hat{n}$ is the normal unit vector pointing outwards from the buoy's surface, dS is the infinitesimal surface area of the buoy, and the red arrows show the pressure field at a few points. In this snapshot, the buoy's draft line is below the free elevation, indicating that the buoy is moving relative to the wave.

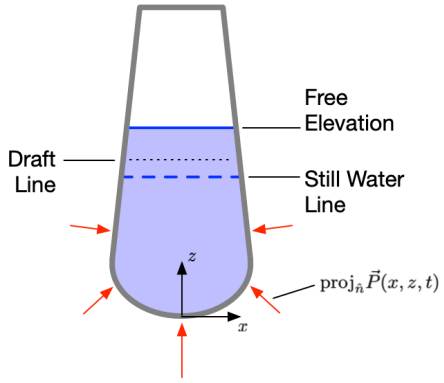

Figure 2. Illustration of the pressure field acting on the buoy over its wetted surface.

To derive a closed-form expression for F_{fk}, it is necessary to obtain an expression for $\vec{P}(x,z,t)$ that can be integrated. The approach used here is the same as that introduced by Giorgi et al. [24] but with three modifications.

1. Consideration of irregular waves of Eq. 1.
2. Inclusion of flat-bottomed buoys.
3. A three-parameter buoy shape.

The pressure applied to the buoy is derived using linear wave theory in the appendix and given by Eq. 5 where ρ is the water density and g is the gravitational acceleration. Eq. 5 assumes that the fluid is incompressible, inviscid, and irrotational with small particle velocities. Furthermore, it's valid only for the portion of the buoy below the SWL unrelated to the wave elevation.

$$P(x,z,t) = \rho \sum_{i=1}^{n} \eta_i(x,t)\, \frac{\omega_i^2}{\chi_i} \frac{\cosh(\chi_i(z+h_w))}{\sinh \chi_i h_w} - \rho g z \tag{5}$$

The dispersion relationship between the wave number, frequency, and depth, $\omega^2 = g\chi \tanh(\chi h_w)$, is also derived in the Appendix and valid under the above mentioned assumptions. If we further assume deep water, $\chi h_w \gg 1$, it can be approximated as $\omega^2 = g\chi$. When applied to Eq. 5, it yields the compact form of Eq. 6.

$$P(x,z,t) = \rho g \sum_{i=1}^{n} \eta_i(x,t)\, e^{\chi_i z} - \rho g z \tag{6}$$

 doi:10.20944/preprints202504.0893.v1

If the wave is regular with a single amplitude, frequency, and phase shift $\phi = \frac{\pi}{2}$, Eq. 6 reduces to the equation used by Giorgi et al. in [24].

$$P(x,z,t) = \rho g e^{\chi z} A \cos(\omega t - \chi x) - \rho g z \tag{7}$$

Finally, it is assumed that the pressure is uniform in x near the buoy, letting us set $x = 0$ in Eq. 6. This is important since it allows for closed-form integration to obtain the FK forces and gives the final form of the pressure field of Eq. 8.

$$P(z,t) = P_d(z,t) + P_s(z) = \rho g \sum_{i=1}^{n} \eta_i(t)\, e^{\chi_i z} - \rho g z \tag{8}$$

where $P_d(z,t)$ and $P_s(z)$ are the dynamic and static pressure components respectively.

3.2. Pressure Integration and Buoy Shape Parameterization

The approach for generating a closed-form expression for F_{fk} is the same as [24], namely, define the buoy shape by a radius $r(z)$ that varies vertically and then integrate the pressure field of Eq. 8 along the radius using cylindrical coordinates. The three additions to the procedure mentioned in Section 3.1 are discussed below. In preparation for a later comparison of FK and buoyancy models, we will write F_{fk} with static and dynamic terms of Eq. 9.

$$F_{fk} = F_{fk,s} + F_{fk,d} \tag{9}$$

using the "s" and "d" subscripts of Eq. 8.

Figure 3 illustrates the notation used in the derivation where $r(z)$ is the revolution profile of the symmetry axis as a function of z that defines the shape of the buoy, θ is the angle of revolution, $\zeta(t)$ is the vertical displacement of the buoy's draft line relative to the still water line (SWL) at $z = 0$, and h defines the draft line relative to a fixed reference of the buoy, in this case, at the bottom of the buoy.

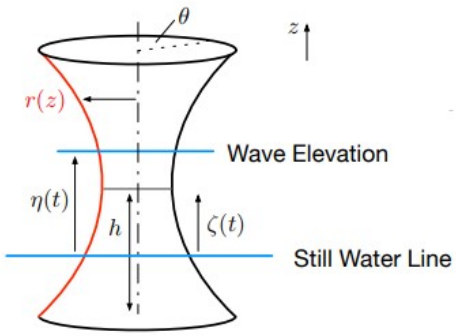

Figure 3. 2D display of the parameters used to derive the forces.

Unlike previous models [24], Eq. 10 is also supplemented by the pressure acting on the base of the buoy, calculated as the product of the base pressure and its area. The cylindrical coordinate rotation limits $[0,\ 2\pi]$ and the vertical limits, $[z_1, z_2]$, are determined by the instantaneous wetted surface below the SWL, or $z_1 = -(h - \zeta)$ and $z_2 = 0$. The buoy's non-uniform cross-sectional plane area is $S(z) = \pi r^2(z)$. Based on these definitions, and utilizing Eq. 4 with considering only the vertical component of $P(z,t)$ due to heave-only-motion, the F_{fk} forces can be calculated as:

$$F_{fk} = F_g + [P_d(z_1,t) + P_s(z_1)]S(z_1) + \int_0^{2\pi}\int_{z_1}^{z_2} [P_d(z,t) + P_s(z)] r(z) r'(z) dz \tag{10}$$

 doi:10.20944/preprints202504.0893.v1

Eq. 10 could be rearranged to obtain the components of the Froude-Krylov (FK) forces as

$$\begin{aligned} F_{fk} =& F_g + S(z_1)P_s(z_1) + \int_0^{2\pi}\int_{z_1}^{z_2} P_s(z)r(z)r'(z)\,dz + \\ & S(z_1)P_d(z_1,t) + \int_0^{2\pi}\int_{z_1}^{z_2} P_d(z,t)r(z)r'(z)\,dz \end{aligned} \tag{11}$$

Substituting Eq. 8 into Eq. 11 and splitting it into static and dynamic components yields Eq. 12.

$$\begin{aligned} F_{fk,s} &= F_g - \rho g\left(S(z_1)z_1 + \int_0^{2\pi}\int_{z_1}^{z_2} zr(z)r'(z)dz\,d\theta\right) \\ F_{fk,d} &= \rho g\left(S(z_1)\sum_{i=1}^{n}\eta_i(t)\,e^{\chi_i z_1} + \int_0^{2\pi}\int_{z_1}^{z_2}\sum_{i=1}^{n}\eta_i(t)\,e^{\chi_i z}r(z)r'(z)dz\,d\theta\right) \end{aligned} \tag{12}$$

Closed-form FK force expressions can be created for a wide range of buoy shapes by introducing a special case of a quadric surface given by Eq. 13 where R is the midline buoy radius and α is the inverse square of the profile slope's asymptote in the vertical direction. Equation 13 limits the buoy shapes to being axisymmetric with circular cross sections.

$$x^2 + y^2 - \alpha z^2 = R^2 \tag{13}$$

Evaluation of Eq. 12 requires the profile equation $r(z)$ obtained from Eq. 13 by shifting the z axis by the buoy displacement ζ and solving for x or y while setting the other variable to zero as shown in Eq. 14.

$$r(z) = \sqrt{R^2 + \alpha(z-\zeta)^2} \tag{14}$$

The area of the circular cross-section is

$$S = \pi r^2 = \pi\left(R^2 + \alpha(z-\zeta)^2\right) \tag{15}$$

and is used to describe the pressure effect on buoy shapes with flat bottoms in Eq. 12. Table 1 summarizes the classes of shapes possible with the parameterization of Eq. 14. The value of α lets the shape range from an oblate spheroid to the hourglass shape of a hyperboloid. The conical shape is a limiting case with zero radius at the midline. This has little practical application for a buoy but provides insight into the effect of the "necking" of the hyperboloid on nonlinear terms in the final differential equation model. Although h is not part of the parameterization of $r(z)$, it is an important parameter to define the vertical height of the buoy.

Table 1. Buoy Shapes and Corresponding Parameters.

Shape	α	R	h
Spheroid, Oblate	< -1	Free	$\frac{R}{\sqrt{-\alpha}}$
Sphere	-1	Free	R
Spheroid, Prolate	$(-1, 0)$	Free	$\frac{R}{\sqrt{-\alpha}}$
Cylinder	0	Free	Free
Hyperboloid (Hourglass)	> 0	Free	Free
Cone-Cone	> 0	0	Free

 doi:10.20944/preprints202504.0893.v1

Three $n \times 1$ arrays, $\boldsymbol{\eta}$, $\boldsymbol{\epsilon}$ and $\boldsymbol{\kappa}$, whose elements are given in Eq. 16 are introduced to make the closed form F_{fk} expression more compact. Note that $\boldsymbol{\eta}$ contains the components η_i, while η is the sum of the components or the free elevation.

$$\eta_i = A_i \sin(\phi_i - \omega_i t),\ \epsilon_i = e^{z_1 \chi_i},\ \kappa_i = \int_{z_1}^{z_2} e^{z\chi_i} r(z) r'(z) dz \tag{16}$$

Substituting Eq. 14 into κ_i and carrying out the integration gives the closed-form expression for κ_i of Eq. 17.

$$\kappa_i = \frac{\alpha}{\chi_i^2}\left[\epsilon_i(1 + h\chi_i) - \chi_i\zeta - 1\right] \tag{17}$$

Substituting $\boldsymbol{\eta}$ and $\boldsymbol{\epsilon}$ from Eq. 16 and $\boldsymbol{\kappa}$ of Eq. 17 into Eq. 12 provides compact expressions for the static and dynamic FK force, which are combined in Eq. 19.

$$\begin{aligned} F_{fk,s} &= -\frac{1}{3}\pi\rho g\zeta\left[3R^2 + \alpha\zeta^2\right] \\ F_{fk,d} &= \pi\rho g\boldsymbol{\eta}^T\left[(R^2 + \alpha h^2)\boldsymbol{\epsilon} + 2\boldsymbol{\kappa}\right] \end{aligned} \tag{18}$$

$$F_{fk} = \frac{1}{3}\pi\rho g\left[3\boldsymbol{\eta}^T\left((R^2 + \alpha h^2)\boldsymbol{\epsilon} + 2\boldsymbol{\kappa}\right) - \zeta(3R^2 + \alpha\zeta^2)\right] \tag{19}$$

While this work focuses on closed-form expressions, it is important to note that $r(z)$ could be any set of points describing an axisymmetric buoy shape. The integrals of Eq. 12 could be computed numerically in real time as the buoy moves. The form of the FK force would be the same except for a modification of the κ_i term.

4. Derivation of F_b

Before developing the F_b model, note that $F_{fk,s}$ of Eq. 18 is indeed a buoyancy force, but it neglects submersion due to wave elevation. This effect is included in the F_b model below.

The total buoyancy force acting on the buoy is

$$F_b = F_g + \rho g V_{sub} \tag{20}$$

where V_{sub} is its submerged volume, calculated as the integral of its varying cross-sectional area $S(r(z))$ over the wetted surface.

$$V_{sub} = \int_{z_1}^{z_2} S(z) dz \tag{21}$$

To account for wave elevation, the area function $S(z)$ and the lower integration bound z_1 are modified from those of Section 3 to include the instantaneous wave elevation and are shown in Eq. 22

$$\begin{aligned} S(z) &= \pi\left(R^2 + \alpha(z + \eta - \zeta)^2\right) \\ z_1 &= -h + \zeta - \eta \end{aligned} \tag{22}$$

Substituting Eq. 22 into the volume integral of Eq. 21, the buoyancy F_b is given in Eq. 23.

$$F_b = \frac{1}{3}\pi\rho g(\eta - \zeta)\left[3R^2 + \alpha(\eta - \zeta)^2\right] \tag{23}$$

5. Model Form Comparison

The difference between Eq. 23 and F_{fk} of Eq. 19 is how wave elevation, η, is used. The F_{fk} expression uses the pressure field containing η_i. However, the boundary conditions of linear wave theory, used to solve Laplace's equation, are applied to the still water line instead of the free elevation, η. This means that the pressure field of Eq. 8 is only valid up to $z_2 = 0$, which is fine as long as both

 doi:10.20944/preprints202504.0893.v1

η and ζ are small. In contrast, the F_b model can be applied to scenarios where both waves and buoy movement are large, though it omits dynamic pressure effects.

Another way to compare F_{fk} and F_b is to write F_b in two parts where the first term is identical to $F_{fk,s}$ of Eq. 18

$$F_b = -\frac{1}{3}\pi\rho g\zeta\left[3R^2 + \alpha\zeta^2\right] + \frac{1}{3}\pi\rho g\eta\left[3R^2 + \alpha(\eta^2 - 3\eta\zeta + 3\zeta^2)\right] \tag{24}$$

and the second term is an alternate representation of $F_{fk,d}$.

To illustrate the differences in the models, Eq. 19 and Eq. 23 are applied to four sample buoy geometries in Table 2 for regular waves, where η has one component. The F_b expressions illustrate the effect of the buoy shape on the nature of the nonlinear contribution to the differential equation model of Eq. 3b. For example, the cylinder is linear in $\eta - \zeta$, whereas the other shapes have a cubic effect. Compared to the linear term, the relative effect of the nonlinearity depends on R and, to some extent, α. The limiting case of the cone-cone shape has no linear term, which means that it has zero stiffness at its equilibrium position with a draft line at its apex. The hourglass shape approximates this behavior for small R.

Table 2. buoyancy model F_b and Froude-Krylov F_{fk} Forces for Different Buoy Shapes in Regular Waves.

Shape	Force Expression
Cylinder 	$F_b = \pi\rho g R^2(\eta - \zeta)$ $F_{fk} = \pi\rho g R^2\left[\eta e^{-\chi(h-\zeta)} - \zeta\right]$
Cone-cone 	$F_b = \frac{1}{3}\pi\rho g\alpha(\eta - \zeta)^3$ $F_{fk} = \frac{1}{3}\pi\rho g\left[3\eta\left(\alpha h^2 e^{-\chi(h-\zeta)} + \frac{2\alpha}{\chi^2}\left((1+h\chi)e^{-\chi(h-\zeta)} - \chi\zeta - 1\right)\right) - \alpha\zeta^3\right]$
Sphere 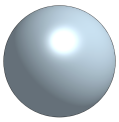	$F_b = \frac{1}{3}\pi\rho g(\eta - \zeta)\left[3R^2 - (\eta - \zeta)^2\right]$ $F_{fk} = \frac{1}{3}\pi\rho g\left[\frac{6}{\chi^2}\eta\left(1 + \chi\zeta - (1 + R\chi)e^{-\chi(R-\zeta)}\right) - \zeta\left(3R^2 - \zeta^2\right)\right]$
Hourglass 	$F_b = \frac{1}{3}\pi\rho g(\eta - \zeta)\left[3R^2 + \alpha(\eta - \zeta)^2\right]$ $F_{fk} = \frac{1}{3}\pi\rho g\left[3\eta\left(\left(R^2 + \alpha h^2\right)e^{-\chi(h-\zeta)} + \frac{2\alpha}{\chi^2}\left((1+h\chi)e^{-\chi(h-\zeta)} - \chi\zeta - 1\right)\right) - \zeta\left(3R^2 + \alpha\zeta^2\right)\right]$

6. Experimental Validation

The two models of Eq. 3 are evaluated below using regular wave experiments. The objective was to compare F_b with F_{fk} without buoy motion, $\zeta = 0$, and then examine the effect of the scattering force F_S.

 doi:10.20944/preprints202504.0893.v1

6.1. Experimental Setup

The tests were carried out at MTUWave, the wave tank laboratory at Michigan Technological University, shown in Figure 4. A spherical buoy with a 10 cm radius was mounted to a dynamometer with a Sensing Systems load cell to measure the vertical force exerted by incoming waves. The range of the load cell was $\pm 222N$ with a maximum error of $\pm 0.556N$ and sampled at 100 Hz. The buoy was positioned to have a midline draft and the load cell output was adjusted to zero Newtons.

Two Edinburgh Designs resistance wave gauges, sampled at 128 Hz, were placed on either side of the buoy, laterally aligned with the center of the buoy. The wave gauge measurements were averaged to estimate the wave elevation at the buoy. The wave gauges were calibrated at five vertical positions, so their uncertainty was approximately 0.5 mm.

A dSPACE MicroLabBox was used to log the load cell and provide a synchronization signal to start the wave maker paddles and wave gauge logging. This allowed for the alignment of the data collected across multiple acquisition platforms.

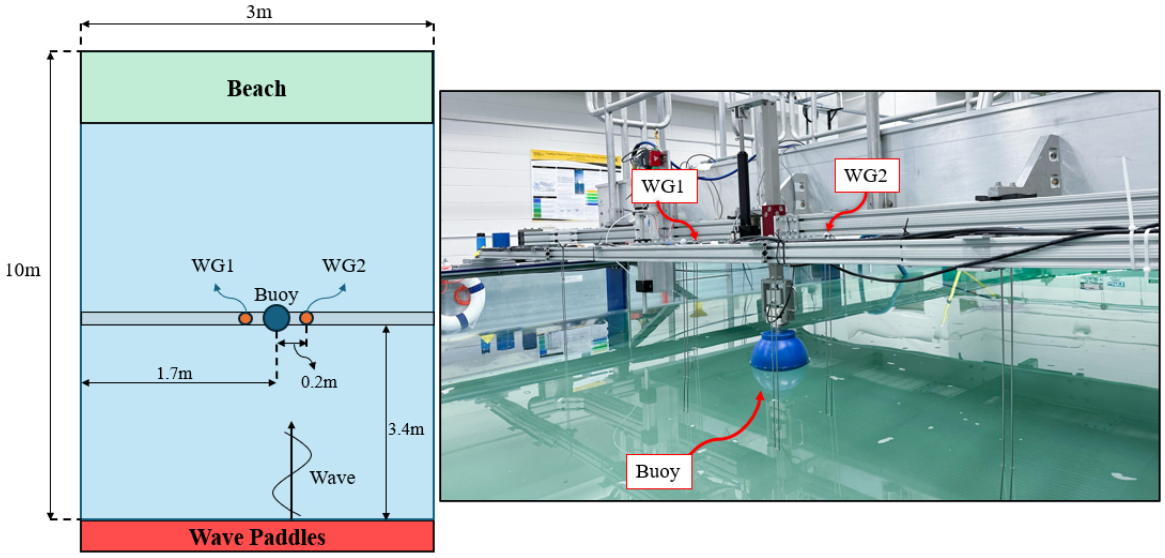

Figure 4. Experimental setup at the Michigan Tech wave tank (MTUWave) with Wave Gauge (WG) positions.

The test conditions are shown in Table 3 and were chosen to exercise the model while not exceeding the capabilities of the wave tank. The nine tests included three different frequencies and amplitudes with wave steepness, the ratio of wave amplitude to wavelength, provided for reference.

Table 3. Regular wave characteristics used for model comparison experiments. The first two columns are the independent parameters, while the remaining columns are for reference.

Frequency f, Hz	Amplitude A, mm	Number χ, 1/m	Length λ, m	Steepness
0.2	[10, 15, 20]	0.4	15.2	[0.0005, 0.0008, 0.001]
0.6	[10, 15, 20]	1.6	4.0	[0.005, 0.007, 0.009]
1.0	[10, 15, 20]	4.0	1.6	[0.013, 0.019, 0.026]

6.2. Data Comparison

Wave elevation measurements, η, were used to calculate F_{fk} and F_b using Eq. 25, taken from the sphere entry of Table 2, where $\zeta = 0$, $\rho = 1000\,\mathrm{kg/m^3}$, $g = 9.81\,\mathrm{m/s^2}$, and $R = 0.1\,\mathrm{m}$.

$$\begin{aligned} F_{fk} &= \frac{2\pi\rho g}{\chi^2}\eta\left[1-(1+R\chi)e^{-R\chi}\right] \\ F_b &= \frac{1}{3}\pi\rho g\eta(3R^2-\eta^2) \end{aligned} \tag{25}$$

 doi:10.20944/preprints202504.0893.v1

The calculated and measured forces are compared in Figures 5–7. Both models perform well at low frequencies, the uppermost plot in Figures 5 through 7. As the frequency of the wave increases, both models overpredict the force; however, the F_{fk} approach outperforms the F_b model.

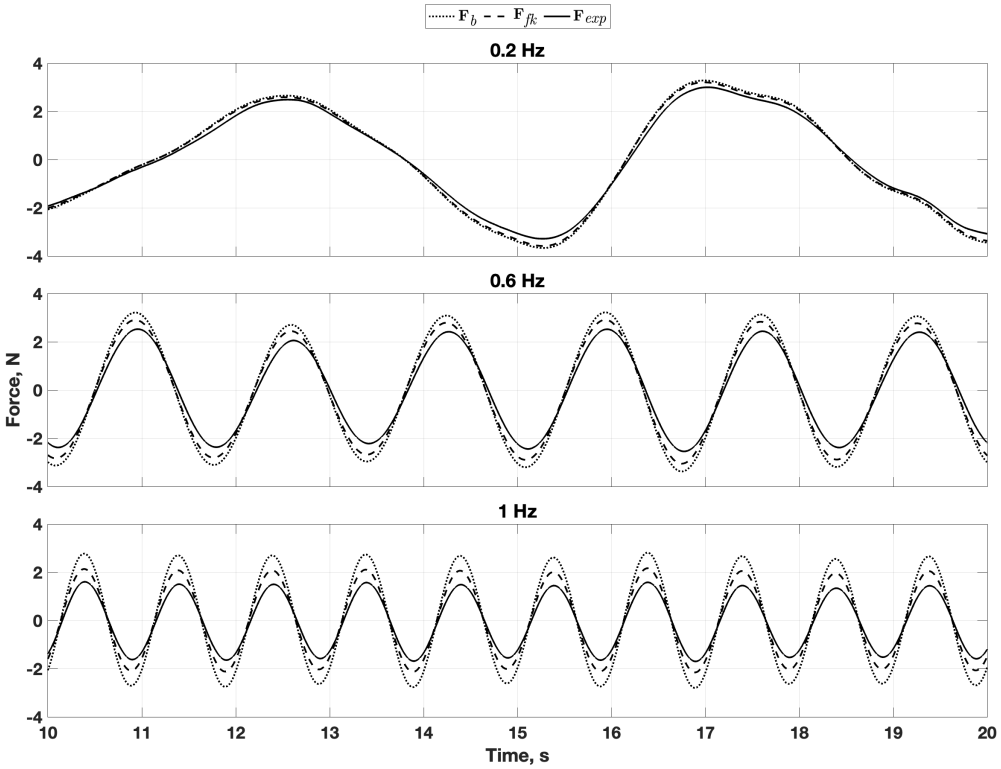

Figure 5. Comparison of measured and modeled buoy forces for $A = 10$ mm at frequencies of 0.2, 0.6, and 1.0 Hz.

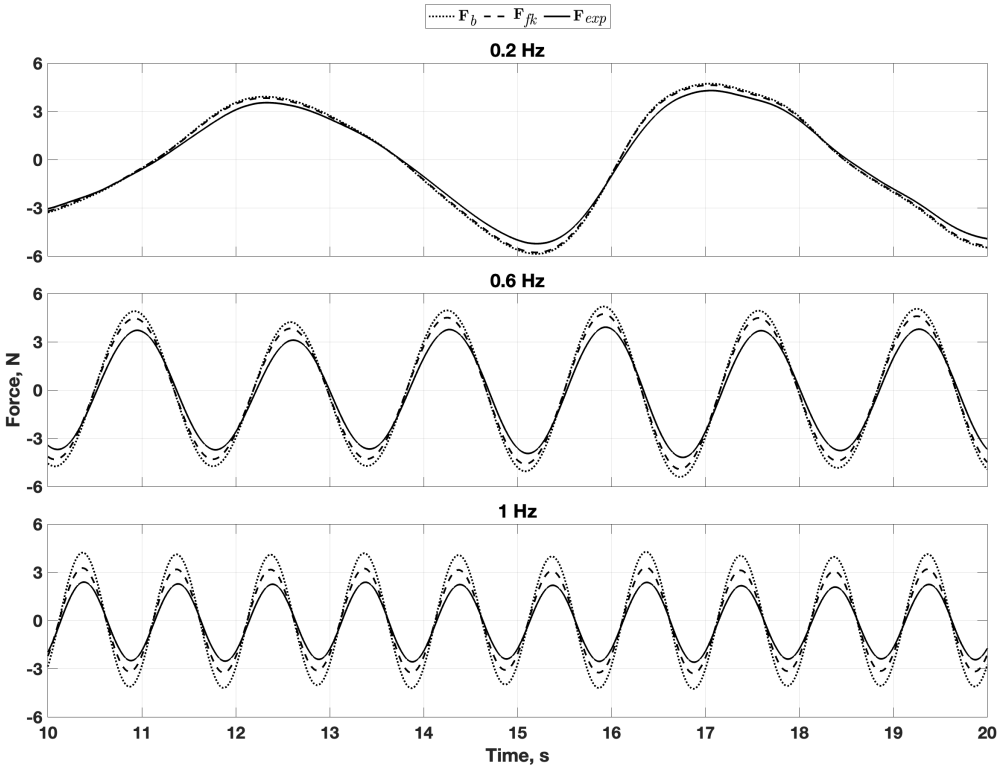

Figure 6. Comparison of measured and modeled buoy forces for $A = 15$ mm at frequencies of 0.2, 0.6, and 1.0 Hz.

 doi:10.20944/preprints202504.0893.v1

The comparison of F_{fk} and F_b with the measured buoy forces ignores the contribution of the scattering force, F_S, of Eq. 3. This force is generally considered negligible when the buoy diameter is significantly smaller than the wavelength [32]. Neglecting F_S aligns well with the 0.2 Hz frequency data, where $\lambda/R \approx 150$ and the difference between the measured and calculated forces is less than 0.5 N for the 20 mm amplitude case. However, neglecting F_S for the 0.6 Hz and 1.0 Hz cases where λ/R is about 40 and 16, respectively, is a possible explanation for the increase in the deviation between the measured and computed forces in the second and third plots in Figures 5 through 7. The maximum deviation for F_b is 1.7 N, and for F_{fk}, it is 0.8 N, both occurring in the 1.0 Hz case of Figure 7.

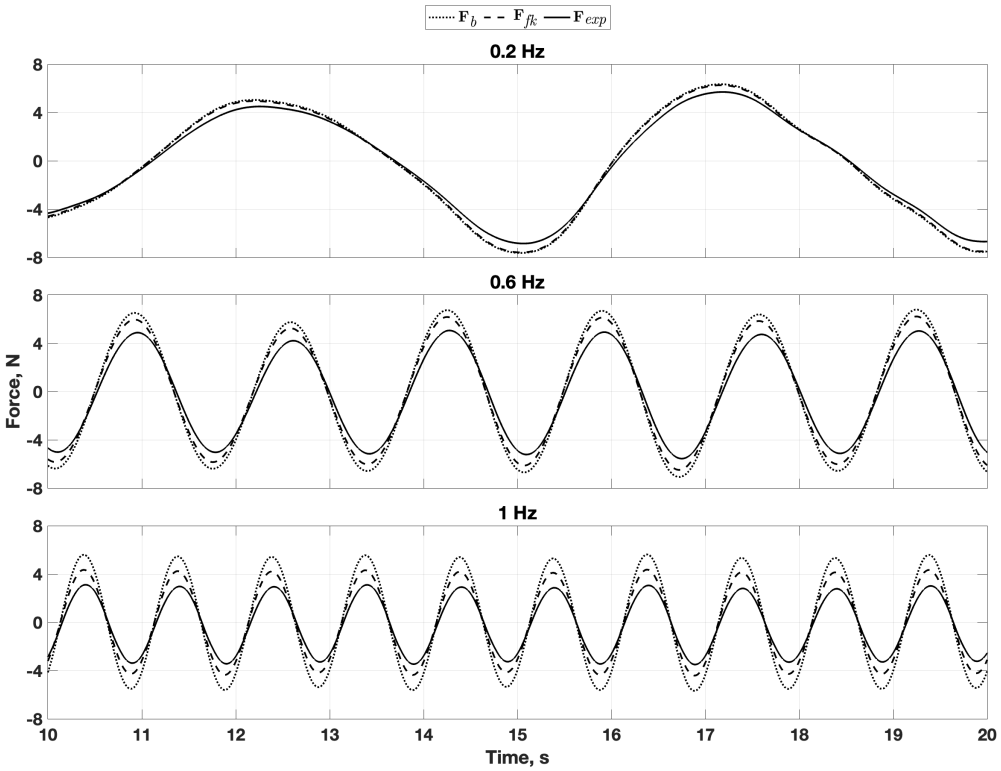

Figure 7. Comparison of measured and modeled buoy forces for $A = 20$ mm at frequencies of 0.2, 0.6, and 1.0 Hz.

The total diffraction force, F_D, is defined as the sum of the scattering and Froude-Krylov forces [33].

$$F_D = F_{fk} + F_S \tag{26}$$

While the Froude-Krylov component can be obtained as described in Section 3, the scattering force can be extracted from the numerical solution of the diffraction problem, [32]. The complex scattering force coefficients, $F_S(\omega)$, were obtained using the boundary element method solver, WAMIT, applied to the spherical buoy using a 972-panel mesh from $\omega = 0.01 - 15$ rad/s in increments of 0.01 rad/s. The real part of $F_s(\omega)$ is shown in Figure 8 and the time domain force used in the model was created using Eq. 27

$$F_S(t) = \mathrm{Re}[F_S(\omega)]\eta(t) \tag{27}$$

for the nine cases of frequencies and amplitudes considered. Eq. 27 is the special case of the irregular wave form, Eq. 28, for a regular wave with a single amplitude, frequency, and phase shift.

$$F_S(t) = \sum_{i=1}^{n} \mathrm{Re}[F_S(\omega_i)]A_i \sin(\phi_i - \omega_i t) = \mathrm{Re}\left[F_S^T(\omega_i)\right]\boldsymbol{\eta}(t) \tag{28}$$

Preprints.org (www.preprints.org) | NOT PEER-REVIEWED | Posted: 11 April 2025 doi:10.20944/preprints202504.0893.v1

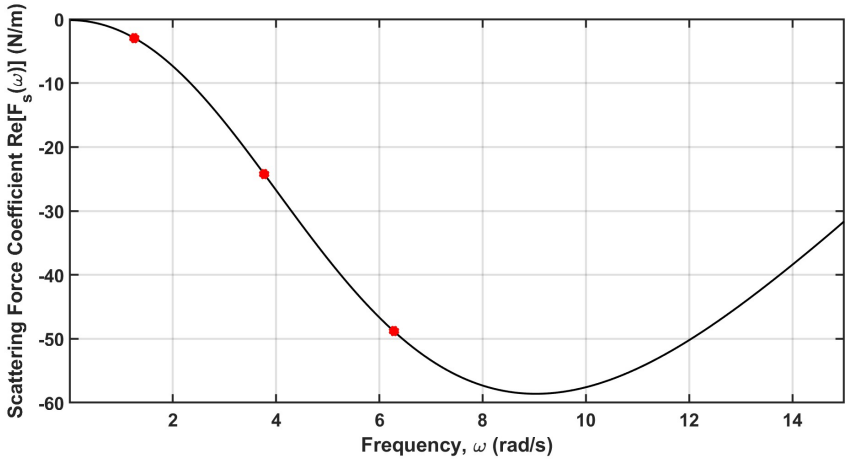

Figure 8. Real scattering coefficient of a 0.1 m spherical buoy. The experiment frequencies of 0.2, 0.6, and 1.0 Hz correspond to 1.3, 3.8, and 6.3 rad/s and are shown with corresponding coefficients of -2.98, -24.23 and -48.82 respectively.

Figure 9 compares the effect on the maximum force error of using the F_s expression of Eq. 27 in the model. Each 3×3 matrix shows the maximum force error between the model and the experiment for three frequencies and three amplitudes. The top two matrices are generated from the data of Figures 5 through 7, and the bottom two matrices show maximum errors between the experiments and the model with F_s. As expected, as the frequency of the wave increases, F_s has a larger effect. It is also readily observed that the F_{fk} model estimates force better than the F_b model as frequency increases. The F_{fk} force is about twice as accurate as the F_b force at 0.6 Hz and four times as accurate at 1.0 Hz.

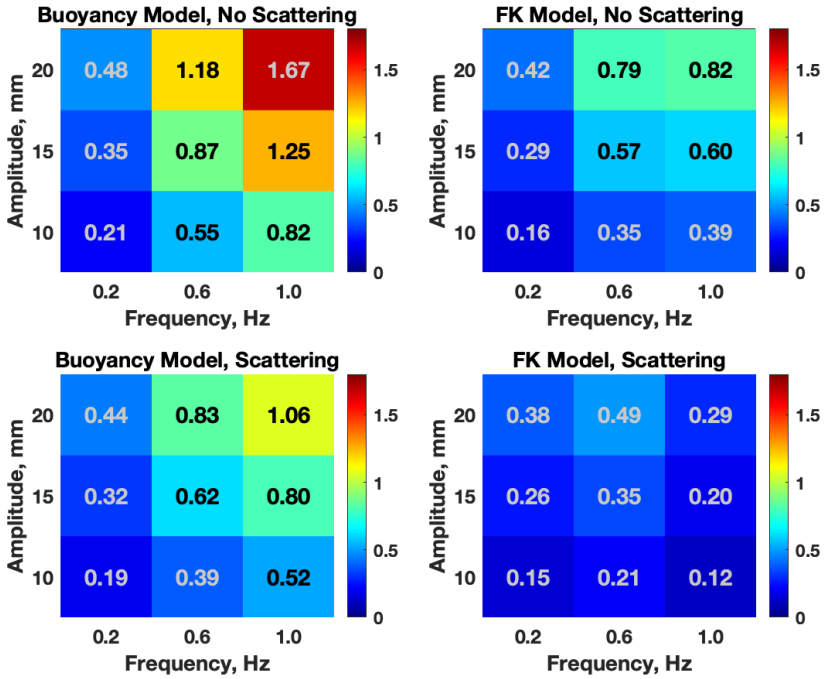

Figure 9. Comparison of the nine experiments with four different models: F_b (upper left), F_{fk} (upper right), $F_b + F_s$ (lower left) and $F_{fk} + F_s$ (lower right). The values in each square are the maximum force difference between the experiment and the model.

As an example, Figure 10 shows the time history comparison of the measured and modeled forces when including F_s, and is a direct comparison to Figure 7.

 doi:10.20944/preprints202504.0893.v1

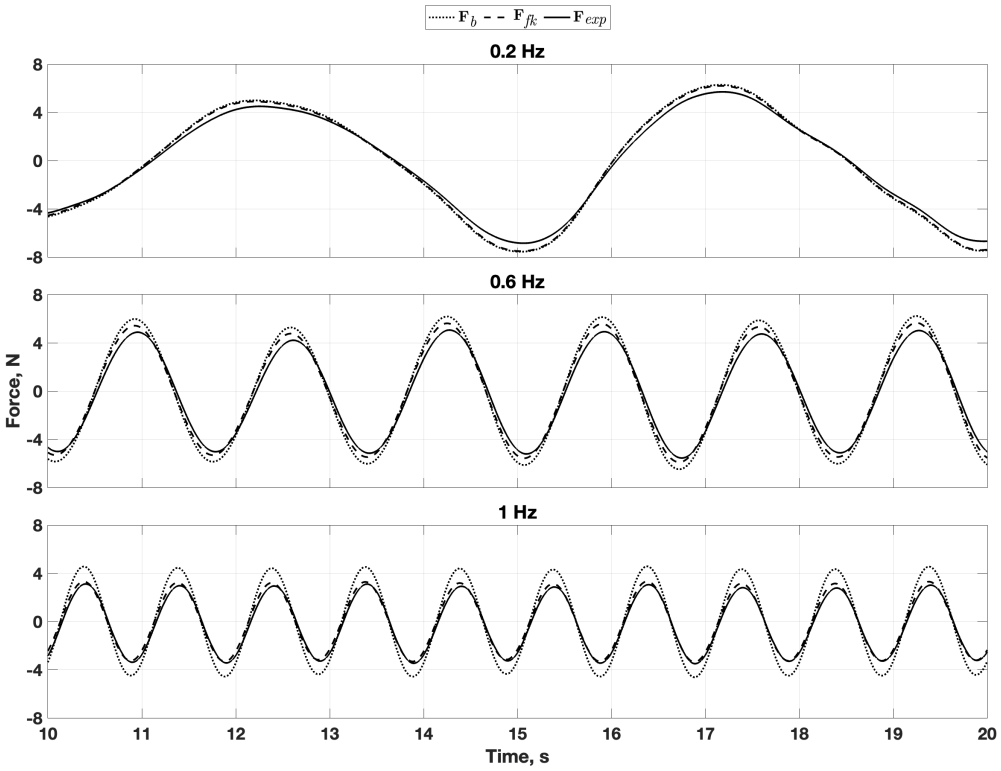

Figure 10. Comparison of measured and modeled buoy forces for $A = 15$ mm at frequencies of 0.2, 0.6, and 1.0 Hz where F_s was included in the model.

7. Conclusion and Future Work

Both the F_{fk} and F_b models contain geometry-induced nonlinearity. The F_{fk} model is based on linear wave theory and is applicable to small wave elevations and motion. In contrast, the F_b model, while not as accurate as the F_{fk} model in small-wave conditions, does not assume small waves and motion as long as the waves are far from breaking. Including a scattering force term improves force prediction even for large λ/R ratios, e.g., 40.

The ability to express F_{fk} using three parameters that span a variety of buoy shapes is convenient for the design of control laws based on the model and possibly the optimization of the shapes.

Irregular wave model validation needs to be performed to further bound the model applicability. Experiments with different buoy shapes and nonlinear control law implementation are additional areas to explore.

Acknowledgments: Sandia National Laboratories is a multimission laboratory managed and operated by National Technology & Engineering Solutions of Sandia, LLC, a wholly owned subsidiary of Honeywell International Inc., for the U.S. Department of Energy's National Nuclear Security Administration under contract DE-NA0003525. This paper describes objective technical results and analysis. Any subjective views or opinions that might be expressed in the paper do not necessarily represent the views of the U.S. Department of Energy or the United States Government.

Appendix A

The pressure expression of Eq. 5 is derived below. The approach closely follows that of Chapter 4 of Newman's Marine Hydrodynamics text [7,33,34] applied to irregular waves.

Consider the situatin of Figure A1 where waves, with free elevation expressed in Eq. A1, propagate along x with no variation in y. The still water line, SWL, corresponds to $z = 0$, and there is a rigid boundary at $z = -h_w$.

 doi:10.20944/preprints202504.0893.v1

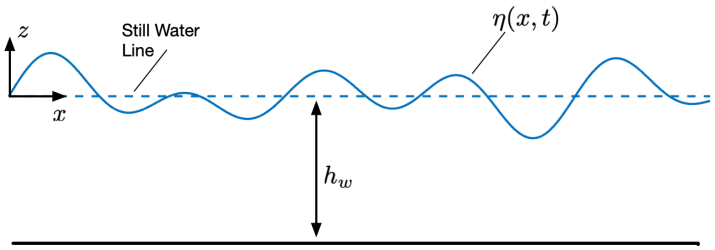

Figure A1. Illustration of an irregular wave.

$$\eta(x,t) = \sum_{i=1}^{n} A_i \sin(\phi_i + \chi_i x - \omega_i t) = \sum_{i=1}^{n} \eta_i(x,t) \tag{A1}$$

Assuming incompressibility the continuity equation is

$$\frac{\partial u}{\partial x} + \frac{\partial w}{\partial z} = 0 \tag{A2}$$

where u and w are the x and z velocity vector components of a fluid particle located at some Cartesian coordinate point (x,z) and are functions of x, z, and t. If the flow is irrotational, the velocities can be expressed in terms of the velocity potential function, $\Phi(x,z,t)$

$$u = \frac{\partial \Phi}{\partial x}, \quad w = \frac{\partial \Phi}{\partial z} \tag{A3}$$

Combining Eq. A2 and Eq. A3 generates the Laplace Equation in terms of the fluid velocity potential.

$$\frac{\partial^2 \Phi}{\partial x^2} + \frac{\partial^2 \Phi}{\partial z^2} = 0. \tag{A4}$$

If we further assume the fluid is inviscid, then the unsteady form of Bernoulli's equation can be developed from the continuum equation as

$$\frac{\partial \Phi}{\partial t} + \frac{1}{2}\left(\left[\frac{\partial \Phi}{\partial x}\right]^2 + \left[\frac{\partial \Phi}{\partial z}\right]^2 + 2\frac{\partial \Phi}{\partial x}\frac{\partial \Phi}{\partial z}\right) = -\frac{1}{\rho}(P + \rho g z) \tag{A5}$$

Now we'll assume the velocities of the fluid particles are small, eliminating the second-order terms of Eq. A5

$$P = -\rho \frac{\partial \Phi}{\partial t} - \rho g z \tag{A6}$$

The $\Phi(x,z,t)$ that satisfies Eq. A4, with suitable kinematic boundary conditions, can be substituted into Eq. A6 to create the pressure field expression of Eq. 5. At this point, we've assumed the flow is incompressible, irrotational, inviscid, with small velocity, but, without any assumption on the wave elevation $\eta(x,t)$.

We'll first consider the kinematic boundary conditions applicable to Eq. A4 based on the z-component of a fluid particle. At the sea floor, the velocity must be zero, giving the boundary condition Eq. A7

$$w = \left.\frac{\partial \Phi}{\partial z}\right|_{z=-h_w} = 0 \tag{A7}$$

and at the free elevation, the fluid particle's z component of the relative velocity

$$w - \frac{d\eta}{dt} = w - \left(\frac{\partial \eta}{\partial t} + \frac{\partial \eta}{\partial x}u\right) = \frac{\partial \Phi}{\partial z} - \frac{\partial \eta}{\partial t} - \left(\frac{\partial \eta}{\partial x}\frac{\partial \Phi}{\partial x}\right) \tag{A8}$$

 doi:10.20944/preprints202504.0893.v1

should be zero. Assuming η is small, the free elevation boundary condition is

$$\frac{\partial \eta}{\partial t} = \left.\frac{\partial \Phi}{\partial z}\right|_{z=\eta(x,t)} \tag{A9}$$

We will solve the Laplace equation using the separation of variables approach with the assumed form of Eq. A10.

$$\Phi(x,z,t) = \sum_{i=1}^{n} c_i(z)\cos(\phi_i + \chi_i x - \omega_i t) \tag{A10}$$

Differentiating Eq. A10 twice with respect to z and x, we obtain

$$\begin{aligned} \frac{\partial^2 \Phi}{\partial x^2} &= -\sum_{i=1}^{n} c_i \chi_i^2 \cos(\phi_i + \chi_i x - \omega_i t) \\ \frac{\partial^2 \Phi}{\partial z^2} &= \sum_{i=1}^{n} \frac{\partial^2 c_i}{\partial z^2} \cos(\phi_i + \chi_i x - \omega_i t) \end{aligned} \tag{A11}$$

Substituting Eq. A11 into Eq. A4, we find that the c_i must satisfy the differential equations of Eq. A12.

$$\frac{\partial^2 c_i}{\partial z^2} - \chi_i^2 c_i = 0 \tag{A12}$$

whose solutions are

$$c_i = a_i e^{\chi_i z} + b_i e^{-\chi_i z} \tag{A13}$$

where the a_i and b_i are constants that can be determined from the boundary conditions.

Consider first the sea floor boundary condition of Eq. A7. The general expression for $\partial\Phi/\partial z$ is

$$\frac{\partial \Phi}{\partial z} = \sum_{i=1}^{n} \frac{\partial c_i}{\partial z} \cos(\phi_i + \chi_i x - \omega_i t) = \sum_{i=1}^{n} \chi_i \left(a_i e^{\chi_i z} - b_i e^{-\chi_i z}\right) \cos(\phi_i + \chi_i x - \omega_i t) \tag{A14}$$

Evaluating Eq. A14 at $z = -h_w$, the only way Eq. A7 will be satisfied for all time is if the coefficient of the cosine term is zero.

$$\sum_{i=1}^{n} (a_i e^{-\chi_i h_w} - b_i e^{\chi_i h_w}) = 0 \tag{A15}$$

Since the χ_i are unique, this becomes n equations where

$$a_i = b_i e^{2\chi_i h_w} \tag{A16}$$

Substituting Eq. A16 into Eq. A13 gives a new version of c_i

$$c_i = 2 b_i e^{\chi_i h_w} \cosh(\chi_i (z + h_w)) \tag{A17}$$

The boundary condition at $z = \eta$, Eq. A9, should be used to obtain an expression for the b_i. However, its reliance on the varying $\eta(x,t)$ makes a closed-form solution elusive at best. Instead, we'll apply Eq. A9 at the SWL, $z = 0$. Chapter 6 of [33] provides a detailed justification of this approximation using the assumption that η is small. This aspect of linear wave theory means that when computing the F_{fk} force of Section 3, the integration of the pressure field should be carried out to the SWL and not the free elevation.

The boundary condition of Eq. A9 requires that

$$\frac{d}{dt}\eta(x,t) = \sum_{i=1}^{n} -A_i \omega_i \cos(\phi_i + \chi_i x - \omega_i t) = \sum_{i=1}^{n} \chi_i b_i (1 - e^{2\chi_i h_w}) \cos(\phi_i + \chi_i x - \omega_i t) \tag{A18}$$

 doi:10.20944/preprints202504.0893.v1

Again, assuming the wave components are independent, we get n equations for the b_i

$$b_i = -\frac{\omega_i}{2\sinh(\chi_i h_w)\chi_i e^{\chi_i h_w}} A_i \tag{A19}$$

Substituting Eq. A19 into Eq. A17 gives the the final expression for c_i as

$$c_i = -\frac{\omega_i}{\chi_i} A_i \frac{\cosh(\chi_i(z+h_w))}{\sinh \chi_i h_w} \tag{A20}$$

and the velocity potential

$$\Phi(x,z,t) = -\sum_{i=1}^{n} \frac{\omega_i}{\chi_i} A_i \frac{\cosh(\chi_i(z+h_w))}{\sinh \chi_i h_w} \cos(\phi_i + \chi_i x - \omega_i t) \tag{A21}$$

Substituting Eq. A21 into Eq. A6 gives the final pressure field

$$P(x,z,t) = \rho \sum_{i=1}^{n} \frac{\omega_i^2}{\chi_i} A_i \frac{\cosh(\chi_i(z+h_w))}{\sinh \chi_i h_w} \sin(\phi_i + \chi_i x - \omega_i t) - \rho g z \tag{A22}$$

As a final note, we can derive the dispersion equation that relates the frequencies of the wave components to their wave numbers. First, a dynamic boundary condition is created from Bernoulli's equation by noting that the pressure at $z = \eta$ should be equal to the atmospheric pressure or

$$\left.\frac{\partial \Phi}{\partial t}\right|_{z=\eta(x,t)} + g\eta(x,t) = 0 \tag{A23}$$

Using the linear wave theory justification of assigning boundaries at the SWL instead of η we have

$$-\sum_{i=1}^{n} \frac{\omega_i^2}{\chi_i} A_i \frac{\cosh \chi_i h_w}{\sinh \chi_i h_w} \sin(\phi_i + \chi_i x - \omega_i t) + g \sum_{i=1}^{n} A_i \sin(\phi_i + \chi_i x - \omega_i t) = 0 \tag{A24}$$

which could be rewritten as

$$\sum_{i=1}^{n} \left(g - \frac{\omega_i^2}{\chi_i} \frac{\cosh \chi_i h_w}{\sinh \chi_i h_w} \right) \sin(\phi_i + \chi_i x - \omega_i t) = 0 \tag{A25}$$

from which we can extract the dispersion equation

$$\omega_i^2 = g\chi_i \tanh(\chi_i h_w) \tag{A26}$$

that is valid as long as it's applied to situations where all the assumptions mentioned previously are appropriate.

References

1. Aderinto, T.; Li, H. Review on power performance and efficiency of wave energy converters. *Energies* **2019**, *12*, 4329.
2. Guo, B.; Wang, T.; Jin, S.; Duan, S.; Yang, K.; Zhao, Y. A review of point absorber wave energy converters. *Journal of Marine Science and Engineering* **2022**, *10*, 1534.
3. Faÿ, F.X.; Henriques, J.C.; Kelly, J.; Mueller, M.; Abusara, M.; Sheng, W.; Marcos, M. Comparative assessment of control strategies for the biradial turbine in the Mutriku OWC plant. *Renewable Energy* **2020**, *146*, 2766–2784.
4. Budar, K.; Falnes, J. A resonant point absorber of ocean-wave power. *Nature* **1975**, *256*, 478–479.
5. Falnes, J. A review of wave-energy extraction. *Marine structures* **2007**, *20*, 185–201.
6. Falnes, J.; Kurniawan, A. *Ocean waves and oscillating systems: linear interactions including wave-energy extraction*; Vol. 8, Cambridge university press, 2020.
7. Korde, U.A.; Ringwood, J. *Hydrodynamic control of wave energy devices*; Cambridge University Press, 2016.

 doi:10.20944/preprints202504.0893.v1

8. Faedo, N.; Pasta, E.; Carapellese, F.; Orlando, V.; Pizzirusso, D.; Basile, D.; Sirigu, S.A. Energy-maximising experimental control synthesis via impedance-matching for a multi degree-of-freedom wave energy converter. *IFAC-PapersOnLine* **2022**, *55*, 345–350.
9. Lattanzio, S.; Scruggs, J. Maximum power generation of a wave energy converter in a stochastic environment. In Proceedings of the 2011 IEEE international conference on control applications (CCA). IEEE, 2011, pp. 1125–1130.
10. Bacelli, G.; Nevarez, V.; Coe, R.G.; Wilson, D.G. Feedback resonating control for a wave energy converter. *IEEE Transactions on Industry Applications* **2019**, *56*, 1862–1868.
11. Yassin, H.; Demonte Gonzalez, T.; Nelson, K.; Parker, G.; Weaver, W. Optimal Control of Nonlinear, Nonautonomous, Energy Harvesting Systems Applied to Point Absorber Wave Energy Converters. *Journal of Marine Science and Engineering* **2024**, *12*, 2078.
12. Zou, S.; Abdelkhalik, O.; Robinett, R.; Bacelli, G.; Wilson, D. Optimal control of wave energy converters. *Renewable energy* **2017**, *103*, 217–225.
13. Abdelkhalik, O.; Darani, S. Optimization of nonlinear wave energy converters. *Ocean Engineering* **2018**, *162*, 187–195.
14. Li, G.; Belmont, M.R. Model predictive control of sea wave energy converters–Part I: A convex approach for the case of a single device. *Renewable Energy* **2014**, *69*, 453–463.
15. Brekken, T.K. On model predictive control for a point absorber wave energy converter. In Proceedings of the 2011 IEEE Trondheim PowerTech. IEEE, 2011, pp. 1–8.
16. Zou, S.; Abdelkhalik, O.; Robinett, R.; Korde, U.; Bacelli, G.; Wilson, D.; Coe, R. Model Predictive Control of parametric excited pitch-surge modes in wave energy converters. *International journal of marine energy* **2017**, *19*, 32–46.
17. Demonte Gonzalez, T.; Anderlini, E.; Yassin, H.; Parker, G. Nonlinear Model Predictive Control of Heaving Wave Energy Converter with Nonlinear Froude–Krylov Forces. *Energies* **2024**, *17*, 5112.
18. Wilson, D.G.; Robinett III, R.D.; Bacelli, G.; Abdelkhalik, O.; Coe, R.G. Extending complex conjugate control to nonlinear wave energy converters. *Journal of Marine Science and Engineering* **2020**, *8*, 84.
19. Richter, M.; Magana, M.E.; Sawodny, O.; Brekken, T.K. Nonlinear model predictive control of a point absorber wave energy converter. *IEEE Transactions on Sustainable Energy* **2012**, *4*, 118–126.
20. Darani, S.; Abdelkhalik, O.; Robinett, R.D.; Wilson, D. A hamiltonian surface-shaping approach for control system analysis and the design of nonlinear wave energy converters. *Journal of Marine Science and Engineering* **2019**, *7*, 48.
21. Giorgi, G.; Ringwood, J.V. Implementation of latching control in a numerical wave tank with regular waves. *Journal of Ocean Engineering and Marine Energy* **2016**, *2*, 211–226.
22. Giorgi, G.; Ringwood, J.V. Nonlinear Froude-Krylov and viscous drag representations for wave energy converters in the computation/fidelity continuum. *Ocean Engineering* **2017**, *141*, 164–175.
23. Faltinsen, O. *Sea loads on ships and offshore structures*; Vol. 1, Cambridge university press, 1993.
24. Giorgi, G.; Ringwood, J.V. Computationally efficient nonlinear Froude–Krylov force calculations for heaving axisymmetric wave energy point absorbers. *Journal of Ocean Engineering and Marine Energy* **2017**, *3*, 21–33.
25. Giorgi, G.; Ringwood, J.V. A Compact 6-DoF Nonlinear Wave Energy Device Model for Power Assessment and Control Investigations. *IEEE Transactions on Sustainable Energy* **2019**, *10*, 119–126. https://doi.org/10.1109/TSTE.2018.2826578.
26. Giorgi, G.; Sirigu, S.; Bonfanti, M.; Bracco, G.; Mattiazzo, G. Fast nonlinear Froude–Krylov force calculation for prismatic floating platforms: a wave energy conversion application case. *Journal of Ocean Engineering and Marine Energy* **2021**, *7*, 439–457.
27. Demonte Gonzalez, T.; Parker, G.G.; Anderlini, E.; Weaver, W.W. Sliding mode control of a nonlinear wave energy converter model. *Journal of Marine Science and Engineering* **2021**, *9*, 951.
28. Yassin, H.; Demonte Gonzalez, T.; Parker, G.; Wilson, D. Effect of the Dynamic Froude–Krylov Force on Energy Extraction from a Point Absorber Wave Energy Converter with an Hourglass-Shaped Buoy. *Applied Sciences* **2023**, *13*, 4316.
29. Penalba, M.; Giorgi, G.; Ringwood, J.V. Mathematical modelling of wave energy converters: A review of nonlinear approaches. *Renewable and Sustainable Energy Reviews* **2017**, *78*, 1188–1207. https://doi.org/https://doi.org/10.1016/j.rser.2016.11.137.
30. Giorgi, G.; Ringwood, J.V. Comparing nonlinear hydrodynamic forces in heaving point absorbers and oscillating wave surge converters. *Journal of Ocean Engineering and Marine Energy* **2018**, *4*, 25–35.
31. WAMIT, Inc. *The State of the Art in Wave Interaction Analysis*, 2023.

 doi:10.20944/preprints202504.0893.v1

32. Korde, U.A.; Ringwood, J. *Hydrodynamic Control of Wave Energy Devices*; Cambridge University Press: Cambridge, 2016. https://doi.org/10.1017/CBO9781139942072.
33. Newman, J.N. *Marine Hydrodynamics*; The MIT Press, 1977. https://doi.org/10.7551/mitpress/4443.001.0001.
34. Dingemans, M.W. *Water wave propagation over uneven bottoms: Linear wave propagation*; Vol. 13, World Scientific, 2000.